EXPERIMENTAL MEASUREMENTS OF THE ANTIMATTER COMPONENT IN COSMIC RAYS

Presented by Guido Barbiellini

Final Version by Guido Barbiellini and Massimo Zalateu

I.N.F.N. Trieste

Trieste University, Trieste, Italy

Representing the WIZARD Collaboration

ABSTRACT

The antimatter component of the cosmic ray flux is mainly due to secondary production from reactions of the primary proton flux on the galactic interstellar medium (ISM). Searches for other sources of antimatter such as primordial black hole (PBH) evaporation, dark matter decay or annihilation, or from antiparticle leakage from far away antigalaxies are of deep interest. In this lecture, the present experimental status of antimatter searches from balloon flight experiments is presented. The near future experiments are illustrated (long-duration balloon flights); the very long-term data-taking detectors to be sent into space are also briefly reviewed.
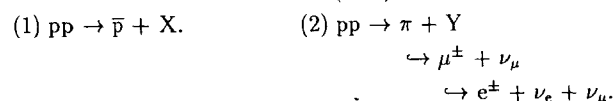
Introduction

The world in which we live and the part of the world we are able to probe with matter seem to be consistent, at the present average temperature, of being composed mainly of the light quarks u and d, and of electrons. These basic components are bound together by the quanta of the strong and electroweak interactions.

The fantaquantities of $\bar{u}$, $\bar{d}$, and e^+ are found at certain given times and in few places in our planet; for instance, you can find antiprotons ($\bar{p}$) or positrons (e^+) at CERN (Geneva), Fermilab (Chicago), SLAC/Stanford, and a few more places in Japan, the USA, and Europe.

In the cosmic rays of our galaxy, there is a sizable amount of $\bar{p}$ and e^+ ($\bar{p}/p \sim 10^{-4}$; $e^+/e^- \sim 10^{-1}$). The amount of known antimatter in our galaxy is compatible with the production mechanisms (1) and (2) from the interactions of primary protons on the interstellar medium (ISM):

(1) $pp \rightarrow \bar{p} + X$.　　　(2) $pp \rightarrow \pi + Y$
$$\hookrightarrow \mu^{\pm} + \nu_\mu$$
$$\hookrightarrow e^{\pm} + \nu_e + \nu_\mu.$$

If the presence of antimatter in our galaxy and others is only that coming from reactions (1) and (2), then some time between the Big Bang and the 100 GeV temperature, a not well-defined interaction has introduced an asymmetry in the baryons as well as in the leptons.

The search for antimatter in the cosmic ray flux is motivated by the following reasons:

1. Search for predictable sources of positrons (e^+) and antiprotons ($\bar{p}$) to test models of galactic interstellar matter and confining mechanisms.

2. Search for possible excess of e^+ and $\bar{p}$ from possible exotic sources: primordial black hole (PBH) evaporation, supersymmetric dark matter candidate annihilation, or decay.

1　The Discovery of Cosmic Rays

Muons are part of the natural background radiation which was discovered early this century. It was assumed to come from the ground, with the intensity therefore decreasing at higher altitudes. It was a great surprise when Victor Hess in his historical balloon flight (Fig. 1) of 1912 discovered that the intensity increased with the altitude. Hess used an electroscope to measure the ionization as a func-

Figure 1: Victor F. Hess in the balloon after one of the first successful flights in which cosmic radiation was discovered.

tion of altitude (results from different electroscope measurements are reported in Table 1). He concluded that the increase could best be explained by penetrating radiation incident on the atmosphere from above. It took some years before this conclusion was generally accepted.

In the tradition of Hess, many more balloon flights have been dedicated to cosmic ray measurements. Studies have been made of the energy spectra and

Altitude (km)	Difference between observed ionization and that at sea-level (ions cm^{-3})
1	−1.5
2	+1.2
3	+4.2
4	+8.8
5	+16.9
6	+28.7
7	+44.2
8	+61.3
9	+80.4

Table 1.

composition. The dominant part (90%) of the cosmic radiation reaching the earth consists of protons. Of the remaining part, 4% is helium, 2% carbon and oxygen, and the rest are heavier elements with a large fraction of iron (if the fluxes are given as particles per GeV per nucleon). The proportions of these components are relatively constant with energy. Their spectra are described by an inverse power law in energy and the differential flux (dN/dE). Figure 2 shows proton cosmic ray energy spectra measured by different flights of the Japan-USA mission BESS.

1.1 Sources of the Antimatter in Cosmic Rays (C.R.)

The predictable amount of antimatter in the C.R. is that due to secondary production from the proton C.R. (see Fig. 2) colliding with the interstellar medium of our galaxy (ISM) and producing secondary pions and antiprotons according to the reactions:

$$p_{CR} + p_{ISM} \rightarrow \pi^{\pm} + X, \qquad p_{CR} + p_{ISM} \rightarrow \bar{p} + Y, \qquad (1)$$

where X and Y are a system of pions and baryons. The pion decay [see Introduction section, production mechanism (2)] induces the positron (e^+) component of the C.R. The main uncertainty on the prediction of the absolute flux of positrons (e^+) and antiprotons ($\bar{p}$) comes from the equivalent amount of ISM seen by the primary protons in the containment time of the secondary e^+ and $\bar{p}$.
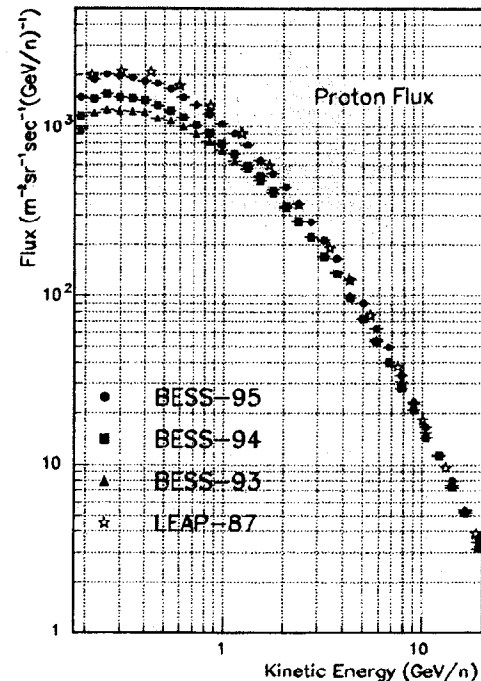

Figure 2: Proton flux measurements in BESS-93, 94, and 95 compared with the LEAP experiment, 1987.

Antimatter is also interesting from the standpoint of cosmology and elementary particle physics. Evidence of primary (not produced in a p-p interaction in the interstellar matter) antiproton components from an extragalactic source would provide the first evidence for large quantities of antimatter in the universe. Furthermore, a primary $\bar{p}$ and e^+ component could also arise from annihilation of dark matter or evaporation of primordial black holes.

2 The Cosmic Ray Positron Component

Measurement of the e^+ component of C.R. started in the early 1970s (Fanselow et al., 1969; Daugherty et al., 1975). The major problems associated with the

balloon-borne positron measurement are:

(a) the e^+ discrimination against the main proton component, and

(b) the correction for e^+ produced in the residual atmosphere and on the top of the balloon.

The very recent data on e^+ in C.R. collected by the CAPRICE Collaboration are reported in the following.

The positron to electron ratio in the cosmic radiation has been measured over more than one decade in energy, from 0.85 to 14 GeV, using the NMSU-WIZARD/CAPRICE balloon-borne magnet spectrometer. The spectrometer uses a solid radiator RICH detector and a silicon-tungsten calorimeter for particle identification. The proton rejection factor of the two instruments combined is better than 2×10^{-6} between 0.6 and 3 GeV/c dropping to 6×10^{-5} at 5 GeV/c and 10^{-4} at 10 GeV/c. The data was collected during 23 hours at a mean residual atmosphere of 4.0 g/cm². From a total of 2756 well-identified e^- and 498 e^+, the positron fraction $R = e^+/(e^+ + e^-)$ as a function of energy has been measured with small errors from 0.85 GeV to 14 GeV for the first time. The energy-dependent behavior of R is consistent with the simple leaky box model of the galaxy. The positron fraction in the upper energy bins are in agreement with the latest high-energy measurements.

2.1 Detector System

Figure 3 shows the NMSU-WIZARD/CAPRICE spectrometer that was flown from Lynn Lake, Manitoba, Canada on August 8, 1994. From top to bottom, it includes a RICH detector (Fig. 4), a time-of-flight (ToF) system, a magnet spectrometer of multiwire proportional chambers (MWPC) and drift chambers (DC), and a silicon-tungsten imaging calorimeter.

The RICH detector (Carlson et al., 1994; Carlson et al., 1995), with a threshold Lorentz factor of 1.5, uses a solid NaF radiator and a photosensitive MWPC with pad readout to detect the Cherenkov light image. It was used to measure the velocity of the particles. The ToF system consists of two layers of plastic scintillators, one above and one below the tracking stack. It was used to give a trigger as well as to measure the time-of-flight and dE/dx losses of the particles. The magnet spectrometer (Golden et al., 1991; Hof et al., 1994) measures the rigidity of the particle with an average maximum detectable rigidity of 200 GeV/c.
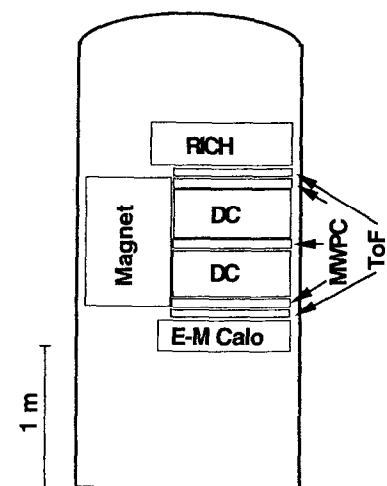

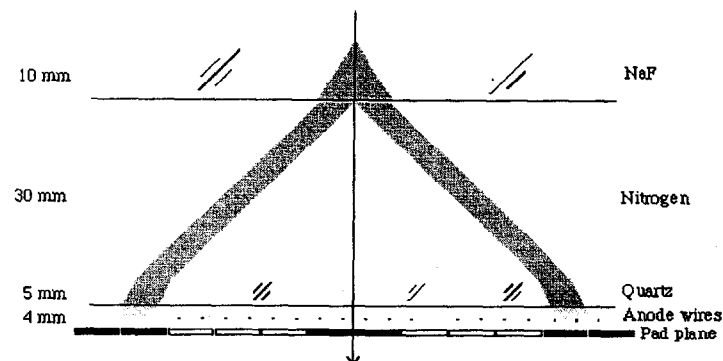Figure 3: A schematic view of the CAPRICE gondola.

Figure 4: A schematic view of the NaF-RICH detector.

Finally, the electromagnetic calorimeter (Bocciolini et al., 1991) is composed of eight planes of double-sided silicon strip detectors interleaved with seven layers of tungsten converters (each one radiation length thick). The silicon strips are placed perpendicular to each other, giving the energy deposited in each strip. Moreover, this imaging device provides information on the longitudinal as well as the lateral profile of the cascade.

2.2 Data Analysis

During the 23-hour-long flight, more than six million events were recorded at a mean residual atmosphere of 4.0 g/cm^2. Electrons and positrons were selected in the rigidity range between 0.6 and 10 GeV/c. Events with a single track having an acceptable chi-square in the tracking of the spectrometer were accepted. The selected singly charged particles give a signal corresponding to less than 1.7 mips (minimum ionizing particles) in the top ToF scintillator. Albedo events were rejected using both the ToF and the RICH. An electron sample was selected as particles with negative deflection, $\beta = 1$ as detected by the RICH and an electromagnetic shower in the calorimeter.

The cuts imposed on the calorimeter to identify electromagnetic showers have a logarithmic dependence on rigidity and are based on (a) results from an experiment using particle beams at CERN (Bocciolini et al., 1993), (b) simulations, and (c) experience gained from a previous flight with the same instrument (Golden et al., 1996). An electromagnetic shower is characterized by a narrow shower with most of the energy deposited inside four Molière radii around the track. Additional cuts based on the total detected energy, which should match the measured momentum, and on the longitudinal and lateral profiles of the shower were applied. A small number of particles emit a bremsstrahlung photon before entering the calorimeter (e.g., in the RICH or the aluminum cover of the gondola) that was detected in the calorimeter as a parallel shower. These double shower events with a single track in the tracking system are clearly electron/positron events and can be used with looser cuts. The detection efficiency of the calorimeter using the above cuts is rigidity dependent increasing from 80% at 0.6 GeV/c to 85% above 0.7 GeV/c, being constant 85% between 0.7 and 3 GeV/c, then slowly decreasing to 75% at 10 GeV/c.

The RICH was used to measure the velocity (β) of the particles. Due to the high rejection factor of the calorimeter, rather loose cuts were applied on the RICH data in order to maximize the efficiency of selection. Electrons and positrons were selected by the RICH as $\beta = 1$ particles with a well-defined Cherenkov light image and a good agreement between the position determined by the RICH and that from the tracking measurement. With these cuts applied, the RICH has a constant detection efficiency of 72% between 0.6 and 5 GeV/c. Above 5 GeV/c, the RICH is not capable of separating protons from positrons and was not used.

The scintillator cut of ≤ 1.7 mip gave an efficiency of 98% for protons, pions, and muons. Electrons and positrons can emit bremsstrahlung photons which materialize in or above the top scintillator. These events will be rejected by the cuts applied. The efficiency for electrons and positrons is found to decrease from 86% at 0.6 GeV to 81% at 10 GeV due to a small increase in shower multiplicity.

2.3 Results

Table 2 gives the number of electrons and positrons that pass the cuts applied on the RICH, the ToF, and the calorimeter. In order to estimate the number of protons which simulate a positron-like cascade in the calorimeter, we selected a proton sample using the RICH and ToF for rigidities less than 1.4 GeV/c. In this energy region, the RICH acts as a threshold counter and the ToF is able to separate protons from lighter particles. Between 1.4 and 5.0 GeV/c, the RICH can accurately identify protons. On this proton sample, the calorimeter cuts were applied and the surviving protons were used to determine the contamination. The proton contamination was found to be 8×10^{-4} for rigidities between 0.6 and 1.0 GeV/c and less than 1×10^{-4} between 1 and 5 GeV/c. In the energy region from 5 to 10 GeV/c, the contamination is assumed to be the same as that of the bin 3 to 5 GeV/c , that is $(1.1 \pm 0.5) \times 10^{-4}$.

The muon and pion background was estimated using Monte Carlo simulations. The pion contamination was found to be 5×10^{-3} below 1 GeV/c and less than 1×10^{-3} between 1 and 5 GeV/c. However, the abundance of pions is less than 1×10^{-3} of the protons at this small atmospheric depth and hence the pion contamination is insignificant. The muon contamination was negligible at all rigidities.

Energy bin at spectrometer GeV	Observed number of events[a] e⁻	e⁺	Extrapolated number at ToP[b] e⁻	e⁺	Atmospheric correction e⁻	e⁺	Median energy at ToA[c] GeV	$\frac{e^+}{e^+ + e^-}$ at ToA[c]
0.6 - 0.8	396	121	886.4	300.4	125.5	184.8	0.99	0.14 ± 0.03
0.8 - 1.05	415	105	905.7	237.6	67.6	94.6	1.30	0.132 ± 0.021
1.05 - 1.5	554	103	1212.6	212.4	45.9	65.9	1.77	0.113 ± 0.014
1.5 - 2.0	447	65	1040.2	139.2	20	26.6	2.45	0.090 ± 0.016
2.0 - 3.0	455	49	1003.4	88.9	14.8	18.1	3.45	0.076 ± 0.012
3.0 - 5.0	303	28(4)	632.5	49.4	7	8.6	5.37	0.075 ± 0.015
5.0 - 10.0	186	27(7)	414.8	43.9	2.9	3.4	9.56	0.07 ± 0.03

[a]The numbers shown in parentheses are the estimated proton background.
[b]Top of payload.
[c]Top of atmosphere.

Table 2: Summary of electron–positron results.

The number of protons passing the RICH cuts was estimated using a proton sample selected by the ToF below 1 GeV/c, and by the calorimeter above 1 GeV/c by requiring a hadronic interaction. The proton contamination in the RICH was found to be 2×10^{-3} between 0.6 and 1 GeV/c increasing to 2% at 3 GeV/c, 30% at 4 GeV/c, and 60% at 5 GeV/c due to the loose cuts applied. It may be pointed out that the RICH cannot separate muons and pions from electrons and positrons in the energy region of interest in this analysis.

Assuming that the rejection of protons by the RICH and the calorimeter is independent, we get a total proton contamination of less than 2×10^{-6} between 0.6 and 3 GeV/c increasing to 6×10^{-5} at 5 GeV/c and 10^{-4} at 10 GeV/c. The rejection factor of the calorimeter and the RICH is high enough to eliminate all proton, pion, and muon contamination from the positron sample between 0.6 and 3 GeV/c. The proton contamination was found to be 9% and 17% of the positron sample in the rigidity bins 3 to 4 GeV/c and 4 to 5 GeV/c, respectively. In the rigidity region 5 to 10 GeV/c, only the calorimeter has been used, resulting in a proton contamination of 25% of the selected positron sample. This proton contamination is shown in the parentheses in Table 2 and was subtracted from the positron sample.

The secondary positrons and electrons, which are produced in the residual atmosphere above the instrument, were estimated in the following manner. We first determined the energy spectrum of the negative muons. These muons were identified by requiring minimum ionizing, negative curvature particles, which enter the instrument from the top and undergo no interaction in the calorimeter. The efficiency of selecting these particles was found to be 98.2%. We show in Fig. 5 the observed spectrum (number of particles per unit energy) of muons from 0.8 GeV to 15 GeV. The dotted curve shown in this figure is the calculated spectrum at 4 g/cm² of residual atmosphere (Stephens, 1981). Note the excellent agreement with data. At the top of the payload (ToP), most secondary electrons and positrons come from decaying muons. We use the normalization constant obtained from the muon spectrum in Fig. 5 to estimate the secondary electron-positron spectra at 4 g/cm² (Stephens, 1981).

The observed electron and positron spectra were corrected for the efficiencies and were extrapolated to the top of the payload using bremsstrahlung corrections. These flux values (particles per unit energy) are shown in Fig. 5 as a function of energy. The estimated atmospheric secondary electrons and positrons are also shown by dashed and solid curves, respectively. The number of secondary particles are tabulated in Table 2 along with the extrapolated number of observed electrons and positrons to the top of the payload.

To check the correctness of this procedure, the growth curve of the electrons in the atmosphere from 4 g/cm² to 200 g/cm² in the energy interval 0.6–0.9 GeV was studied. By normalizing the calculated growth curve (Daniel and Stephens, 1974) for 700 MeV electrons over the depth between 30 and 150 g/cm², the fraction of secondary electrons turns out to be 13.2±1.9% at 4 g/cm². From Table 2, one can estimate that the fraction of secondary electrons in the energy interval between 0.6 and 0.8 GeV is 15.1±2.3%, assuming a possible 15% uncertainty for the theoretical estimate. This observed consistency between these two independent methods gives us confidence that the corrections made are reliable.

The corrected electron and positron spectra were extrapolated to the top of the atmosphere (ToA) by solving simultaneously the cascade equations describing the propagation of electrons, positrons, and gamma rays that result from bremsstrahlung of the electron component. From this, we obtained the positron to electron ratios that are shown in Table 2 along with the median energy at the top of the atmosphere.
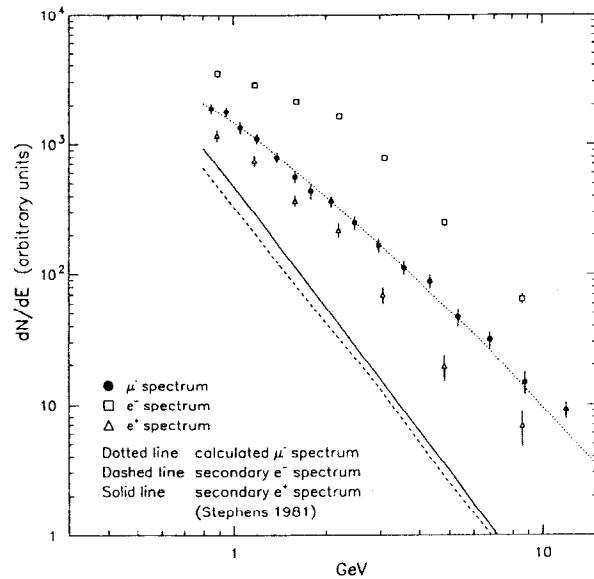
Figure 5: The measured electron and positron flux at the top of the payload, the analytically determined atmospheric background, and the measured muon spectrum with an analytical prediction.

The resulting positron to electron ratio is plotted in Fig. 6 together with previous measurements (Fanselow *et al.*, 1969; Daugherty *et al.*, 1975; Muller and Tang, 1987; Golden *et al.*, 1987; Golden *et al.*, 1994; Barwick *et al.*, 1995; Golden *et al.*, 1996; Agrinier *et al.*, 1969; Clem *et al.*, 1995). The errors shown include both the statistical and the systematic errors. Our results are in agreement with the recent measurements (Golden *et al.*, 1996; Barwick *et al.*, 1995) at the upper energy bins. The positron fraction (R) decreases from 0.14 at 0.8 GeV to 0.075 at 4 GeV and remains nearly constant above this energy. The observed energy dependence of the CAPRICE results is consistent with that expected from the simple leaky box model (Protheroe, 1982). The value of the ratio is dependent on the amount of matter traversed in the interstellar space and on the assumed spectrum of electrons; both of these have large uncertainties. It is essential to obtain the absolute spectra of both electrons and positrons to derive useful information on the origin and propagation of these components. The analysis to obtain absolute fluxes of electrons and positrons is in progress as well as efforts to extend the analysis to lower energies.

3 The Cosmic Ray Antiproton Flux

Antiproton searches started a long time ago following an original idea of L. Alvarez that suggested the possibility of flying a magnetic spectrometer using superconducting coils. Due to the small amount of $\overline{p}$ in C.R. ($\overline{p}/p \sim 10^{-4}$) and because of the large electron background, the progress in this field of C.R. has been quite slow in the past. Recent balloon missions using the most advanced techniques developed in the particle accelerators have improved substantially the experimental status of the art. But for the most relevant progress, future space-based missions are strongly needed. Data from two balloon flight collaborations (CAPRICE and BESS) will be reported in the following.

3.1 CAPRICE Flight 94 for $\overline{p}$ Search

The NMSU-WIZARD/CAPRICE spectrometer described previously for the e^+ data has also collected $\overline{p}$ data.
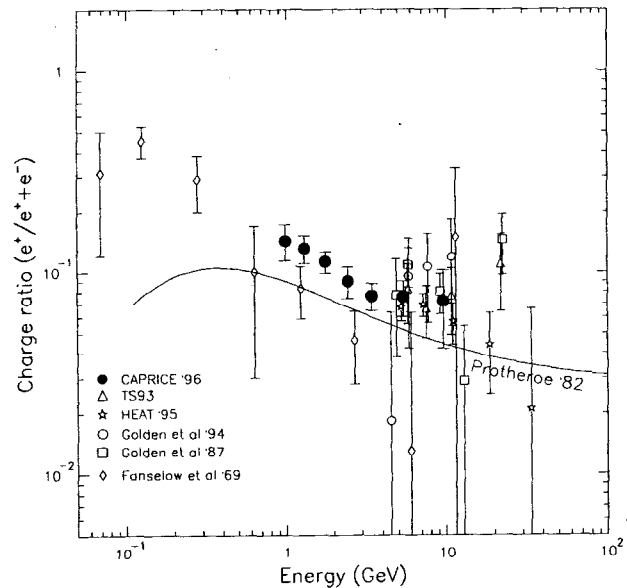
Figure 6: Positron fraction $e^+/(e^+ + e^-)$ as observed in this experiment compared with other published data and a simple leaky box model.

For this data, the 50×50 cm^2 RICH detector (Carlson *et al.*, 1994) is essential; other equipment such as time of flight and the imaging calorimeter enhance the antiproton signal among the more copious negative particles e^-, μ^-, ...

3.1.1 Data Analysis

The analysis was based on 18 hours of data collection for a total acquisition time of 60520 seconds under an average residual atmosphere of 4 g/cm^2.

The data analysis must use the information available from the different detectors to safely identify the antiprotons in a very large background of other particles. Albedo particles, as well as the large number of protons and electrons, must be rejected in the antiproton analysis. About 4% of the cosmic ray protons interact in the atmosphere above the spectrometer and produce π^- and μ^- that must be rejected. Interactions in the spectrometer and associated bar structure also results in a background of negatively charged particles. The remaining background in the antiproton sample is carefully estimated using experimental data and simulations. The selection of protons is more straightforward with little background to reject.

Based on the ability of the RICH to reliably identify antiprotons from pions, muons, and electrons, the rigidity range chosen for our analysis was 1.2 to 4.0 GeV/c. This rigidity bin was divided into two: 1.2 to 2.8 GeV/c and 2.8 to 4.0 GeV/c. At 1.2 GeV/c, the RICH (anti)proton selection efficiency becomes higher than 50%. At a rigidity of 2.8 GeV/c, the Cherenkov angle of (anti)protons becomes less than six standard deviations away from the Cherenkov angle of the β (velocity) ~ 1 particles (pions, muons, and electrons). Four GeV/c is the rigidity where the (anti)proton Cherenkov angle becomes less than three standard deviations away from the Cherenkov angle of $\beta \sim 1$ particles. The results are shown in Table 3.

For the first time, the combination of an electromagnetic calorimeter and a ring imaging Cherenkov detector has been used to measure the cosmic ray flux of antiprotons. This combination has made it possible to accurately identify antiprotons in the presence of a large background of lighter, negatively charged particles. It also allows an accurate determination of the contamination within the antiproton sample.

The flux of antiprotons and the ratio of antiprotons to protons increase over the kinetic energy interval 0.6 to 3.2 GeV, see Table 4. In agreement with

other recent data (e.g., Mitchell *et al.*, 1996), it supports the conjecture that the antiprotons in this energy range are produced in the interstellar medium by primary cosmic rays colliding with interstellar gas.

The combination of all available data on the ratio in the energy range 0.3 to 3 GeV (Moiseev *et al.*, 1996; Bogomolov *et al.*, 1987 and 1990; Mitchell *et al.*, 1996; and this work) shows an increase with energy in agreement with calculations by Gaisser and Schaefer (1992). However, the combined data do not rule out a faster increase than calculated. The two measurements that have been reported above 4 GeV by Golden *et al.* (1984) and by the MASS91 experiment (Hof *et al.*, 1996) differ by about three standard deviations, and further measurements are clearly needed in order to rule out any exotic antiproton production. Fortunately, new experiments are in progress.

3.2 Selection Criteria to Identify p̄ in CAPRICE Data

3.2.1 Scintillators

Particles with charge one were selected using the measured energy loss in the top scintillator. From the observed distribution of the dE/dx as a function of rigidity, singly charged proton-like events were selected in the following manner.

3.2.2 RICH

The RICH was used to measure the Cherenkov angle of the particle and thereby its velocity. The velocity and the Cherenkov angle resolution which depends on the incidence angle, were determined using a large number of protons selected by

Rigidity at spectrometer		Observed number of events[a]		Extrapolated number at top of payload		Atmospheric correction		$\frac{\bar{p}}{p}$ at TOA[b]
GeV/c	p̄	p	p̄	p	p̄	p	
1.2 - 2.8	4(1)	124658	8.6	303433	1.5	8484	2.5 (+3.2,-1.9) ×10⁻⁵
2.8 - 4.0	5(0.7)	25260	17.7	90451	1.4	1662	1.9 (+1.6,-1.0) ×10⁻⁴

[a]The numbers shown in the parentheses are the estimated muon, pion, and electron background.
[b]Top of the Atmosphere. The quoted errors are a combination of statistical and systematic errors.

Table 3: Summary of proton-antiproton results.

Kinetic Energy at TOA[a] GeV	Geometrical factor (m² sr)⁻¹	Antiproton flux at TOA[b] (m² sr s GeV)⁻¹	Proton flux at TOA[b] (m² sr s GeV)⁻¹
0.6 - 2.0	179.1 ± 2.8	1.9 (+2.4, -1.4) ×10⁻²	743 + 17
2.0 - 3.2	177.5 ± 2.8	5.3 (+4.5, -2.9) ×10⁻²	278 ± 10

[a]Top of the Atmosphere.
[b]The quoted errors are a combination of statistical and systematic errors.

Table 4: Antiproton and proton fluxes at the top of the atmosphere.

the calorimeter and the scintillators. The resolution varied from 8 mrad (perpendicular incidence and $\beta \sim 1$) to about 23 mrad (10° off perpendicular incidence and $\beta = 0.78$). Since the RICH is the only detector capable of clearly identifying antiprotons against a background of muons, pions, and electrons in the rigidity range 1.2 to 4 GeV/c, strict cuts were applied on the RICH data. A good agreement between the particle's impact position as determined by the RICH and the tracking system was required. The difference in x and y should be less than three standard deviations (rigidity dependent), typically < 5 mm. Using these conditions, reliable Cherenkov angle information was obtained.

3.2.3 Calorimeter

The calorimeter was used to identify electromagnetic showers. The longitudinal and transverse segmentation of the calorimeter combined with the measurement of the energy lost by the particle in each silicon strip resulted in high identification power ($\sim 85\%$) for electromagnetic showers combined with a high rejection power ($\sim 10^4$) for hadronic particles (Barbiellini *et al.*, 1996). In the analysis presented in this paper, the calorimeter was used to reject events with electromagnetic showers initiated by a single electron, possibly accompanied by a bremsstrahlung photon emitted in the RICH or in the dome above the detector stack (see Weber, 1996 for a description of the selection criteria).

Figures 7 and 8 illustrate the calorimeter performance, and show schematic views of two single events in the CAPRICE apparatus. The instrument is shown in the bending (x) view and in the nonbending (y) view. From top to bottom is displayed: the RICH seen from above, the tracking stack of multiwire proportional chambers and drift chambers, and the imaging calorimeter. Note that Figs. 7
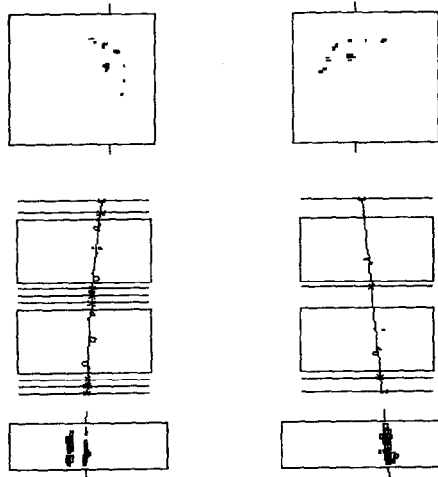
Figure 7: Display of a single 1.3 GeV/c electron traversing the CAPRICE apparatus.

and 8 are not to scale; the calorimeter is significantly thinner than shown in the figure. Figure 7 shows a single 1.3 GeV/c electron traversing the apparatus and emitting a bremsstrahlung photon in the RICH. The RICH shows the detected Cherenkov light image where the ionization of the chamber gas by the electron is shown as a cluster of pads hit in the center surrounded by the signals from the Cherenkov light. Due to total reflection in the NaF crystals, only part of the Cherenkov ring is detected. The tracking stack shows the trajectory of the electron as it is deflected by the strong magnetic field. The calorimeter shows the two electromagnetic showers produced by the electron and the bremsstrahlung photon, respectively. The origin of the bremsstrahlung photon can be located by projecting backward the direction of the shower and determining where it intersects the electron trajectory. More than one-fourth of the electrons in the rigidity region 1.2 to 4 GeV/c were accompanied by a bremsstrahlung photon reconstructed in the calorimeter.

Similarly, Fig. 8 shows a single 2.2 GeV/c antiproton traversing the instrument. The ring of Cherenkov light is clearly seen in the RICH, giving an accurate velocity determination for the particle. The rigidity is measured from the deflection in the
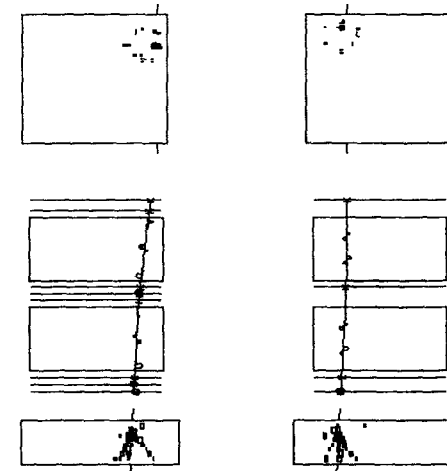

Figure 8: Display of a single 2.2 GeV/c antiproton traversing the CAPRICE apparatus. The antiproton interacts in the calorimeter showing clearly several charged particles emerging from the vertex of interaction; this could be an annihilation in flight.

tracking system. The antiproton interacts in the calorimeter, clearly showing many charged particles emerging from the vertex of interaction; this could be an in-flight annihilation. The interaction probability for a 2.2 GeV/c antiproton is about 40%.

3.2.4 Tracking

The tracking information must be carefully used to eliminate positively charged particles (protons) that have scattered in the tracking system and therefore look like negatively charged particles. Events with more than one track must also be eliminated. To achieve this goal, a set of conditions were imposed on the fitted tracks. These conditions represent a compromise between rejection power and efficiency, and are partly based on experience gained previously using the same tracking system (Mitchell *et al.*, 1996; Hof *et al.*, 1996).

4 BESS-93 to BESS-95 Flights

The largest sample of $\bar{p}$ in C.R. collected so far is the one obtained by the magnetic spectrometer built by the BESS Collaboration.

The BESS experiment has been carried out as a joint research project of the University of Tokyo, National Laboratory for High Energy Physics (KEK), Kobe University, Institute of Space and Astronautical Science (ISAS) in Japan, and National Aeronautics and Space Administration (NASA), New Mexico State University (NMSU), and the University of Maryland in the United States to search for cosmic ray antiparticles and to make precise measurements of cosmic ray spectra.

The BESS spectrometer has been developed since 1987, and three successful scientific flights have been carried out in Canada since 1993.

4.1 BESS Spectrometer and Flights

Figure 9 shows cross sections of the BESS spectrometer. The first two flights were made with configuration (a), and the third flight in 1995 was carried out with configuration (b) after the upgrade of TOF counters with a new pressure vessel. Table 5 gives the latest major spectrometer parameters.

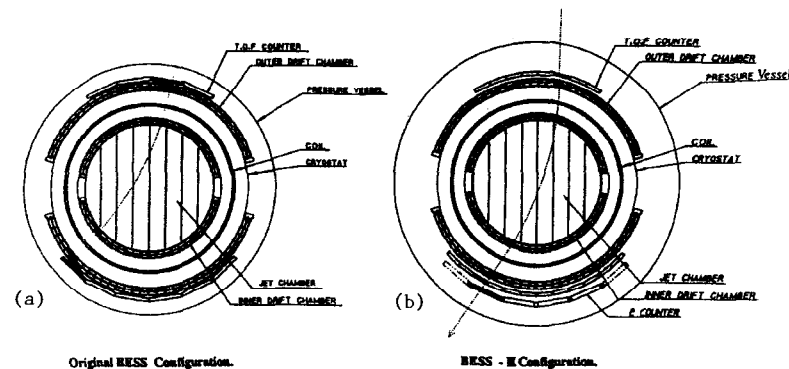The BESS spectrometer was launched by using 29 MCF balloons, in summers since 1993.

Figure 9: Cross sections of BESS spectrometer.

Geometrical Acceptance	0.4 m^{2}sr
Maximum Detectable Momentum	200 GeV/c
Momentum Region for Antiproton Search	2 GeV/c ($\gg$ 3 GeV/c)
Momentum Region for Antihelium Search	50 GeV/c
Trigger Rate	1 - 2 kHz
Event Recording Rate	100 - 200 Hz
Sensitivity for Antiparticle Search	10^{-6} - 10^{-7}/one day flight
Transparency of Half Detector Wall	7.5 g/cm^2
Size of Pressure Vessel	1.7 m$\oslash$ × 3.6 m
Weight of Payload	2.2 ton
Power Consumption	1.2 kW

Table 5: Main parameters of BESS Spectrometer (II).

4.2 Summary and Further Improvements for Future Flights

The BESS spectrometer has detected more than 40 low-energy antiprotons with precise energy measurement and has resulted in bringing the upper limit of the antihelium to helium ratio down to 2×10^{-6}.

Figures 10 and 11 show the BESS-93 results on the $\bar{p}$ flux and the $\bar{p}/p$ ratio. By making an important improvement in the TOF system, the BESS-95 flight has enlarged the momentum interval for $\bar{p}$'s, consequently increasing the statistics available on the world $\bar{p}$ sample. Figure 12 shows the clean $\bar{p}$ sample in the plane $1/\beta$ versus rigidity (β is the $\bar{p}$ velocity in units of c). Figure 13 and Table 6 give the results on the $\bar{p}$ flux in five and four energy bins.

Energy, MeV	$\bar{p}/p$ ratio	Antiproton flux
200-500	1.3×10^{-5}	0.016
500-700	1.2×10^{-5}	0.013
700-1000	1.6×10^{-5}	0.012
1000-1200	3.3×10^{-5}	0.019

Table 6: Results of the 1995 flight.

4.3 BESS Search for Antihelium

All helium events were carefully checked for an antihelium. Event #1,656,905 from the '95 flight showed good parameters, but unfortunately did not have good consistency of the Z coordinate measured by TOF and by the tracking system, and had a sign of interaction above upper IDC. It does not allow us to accept this event as the first detected nonhydrogen antinucleus.

The BESS Collaboration has computed an $\overline{He}$ limit on the basis of the '93-'94 data.

The presence of the $\overline{He}$ in the cosmic ray would be an important discovery implying the existence of primary antimatter within the universe.

Figure 14 shows the rigidity distribution of the detected cosmic rays. From the absence of candidates with negative charge, the limit shown in the following figure is derived. BESS is planning an infrared detector flight in '97 and possible long-duration flights in '99 and later.
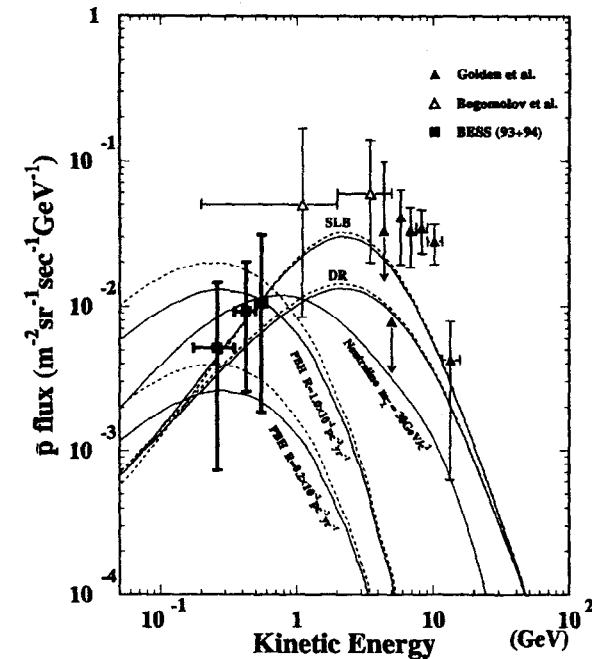

Figure 10: Measured $\bar{p}$ flux in comparision with the results of other experiments and calculations. Filled squares, the present results; filled triangles, Golden et al.; open triangles, Bogomolov et al. The curves labeled "SLB" and "DR" are recently calculated by Mitsui based on the Standard Leaky Box Model and Diffusive Re-acceleration Model, respectively. The dashed curves are for the minimum solar modulation and the solid are for $\phi = 600$ MeV. The curves labeled "PBH" are calculations by Maki et al. on the $\bar{p}$ production by primordial black holes for two values of evaporation rate R. The dashed and solid curves are again for the minimum and $\phi = 600$ MeV solar modulations. The curve labeled "Neutralino" is calculated by multiplying the model of the proton flux and the $\bar{p}/p$ ratio by Jungman and Kamionkowski based on the $\bar{p}$ production by annihilations of dark matter neutralinos.
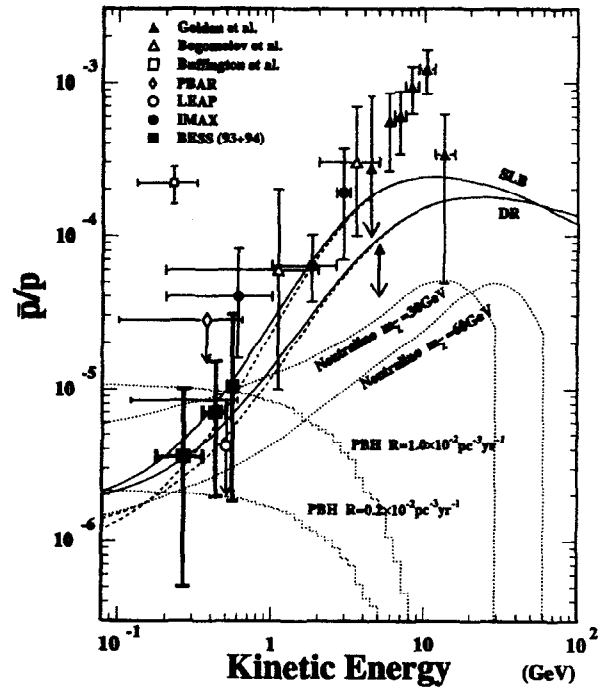
Figure 11: Measured p̄/p ratio in comparision with the other experimental data and calculations. Filled squares, the present result; filled triangles, Golden *et al.*; open triangles, Bogomolov *et al.*; open square, Buffington *et al.*; open diamond, the PBAR experiment; open circle, the LEAP experiment; filled circles, the recent result of IMAX. The dashed curves labeled "SLB" and "DR" are recently calculated by Mitsui based on the Standard Leaky Box Model and Diffusive Reacceleration Model, respectively. The dotted curves labeled "PBH" are predictions of Maki *et al.* for the p̄'s produced by primordial black holes with two different assumed evaporation rates R. The dotted lines labeled "Neutralino" are the prediction of Jungman and Kamionkowski for the p̄ productions by annihilations of dark matter neutralinos.
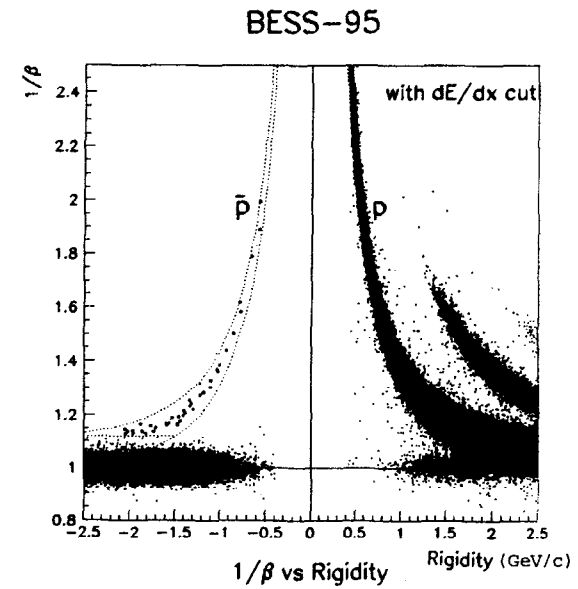
Figure 12: The identification of antiproton events after the dE/dx cut. The antiproton events are marked as solid dots.
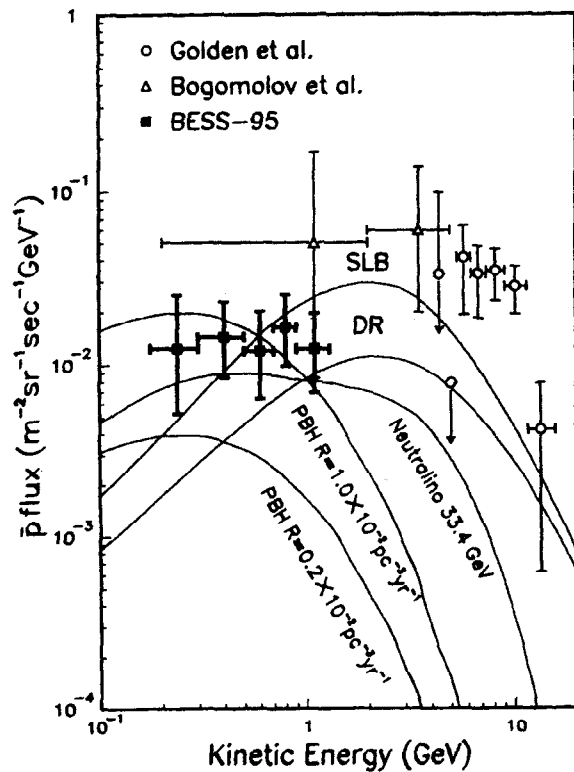
Figure 13: Comparision of the measured p̄ flux with the other experiments and theoretical values. Filled squares, the present result; open circles, Golden *et al.*; open triangles, Bogomolov *et al.* The curves labeled "SLB" and "DR" are calculated by Mitsui based on the Standard Leaky Box Model and Diffusive Re-acceleration Model, respectively. The curves labeled "PBH" are calculated by Maki *et al.* for the p̄ production by primordial black holes. The curve labeled "Neutralino" is calculated by Jungman and Kamionkowski based on the p̄ productions by annihilations of dark matter neutralinos.
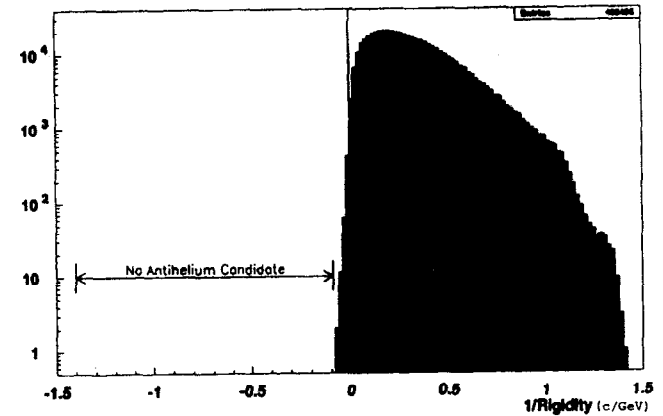
Figure 14: 1/Rigidity distribution.

The expected p̄ results from the future activity are shown in Fig. 15. A very comprehensive presentation of the BESS results are published in the *Proceedings of the 6th Workshop on BESS* published as KEK Proceedings 96-9.

4.4 Future

The BESS long-duration flight expectations should lead to an impressive improvement in the experimental knowledge of antimatter within cosmic rays. But the most important step forward is expected to come from future space experiments. Long duration in this case means more than three years, so statistics can increase largely even with an effective area of reduced dimension.

But the experiments in space also benefit from the absence of a residual atmosphere on top of the detector, which introduces an unavoidable background for balloon-borne experiments.

Two projects searching for antimatter in space are in a stage of advanced construction. The basic principles are similar, both using as a basic element a magnetic spectrometer with a permanent magnet to give the magnetic field inside a region where high space accuracy trackers (Si trackers) are inserted. The basic
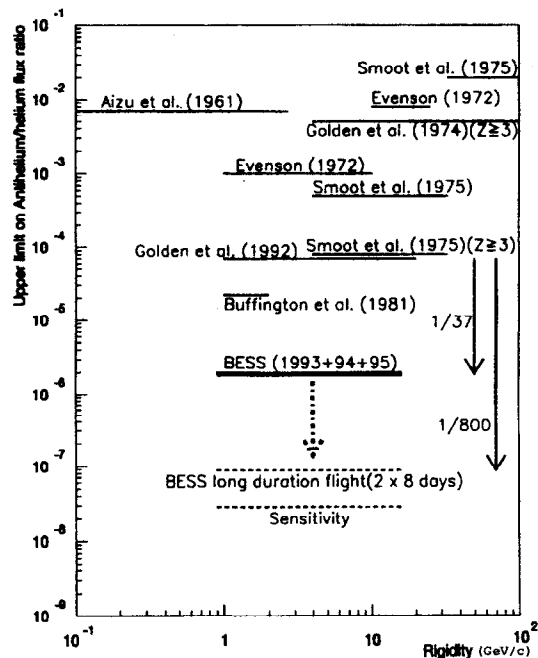
Figure 15: Upper limit on $\overline{\text{He}}$/He flux ratio.

elements of the two experiments are implemented in different ways by particle identification detectors.

The AMS spectrometer will be located in the International Space Station Alpha (ISSA) after a flight test in the shuttle scheduled for 1998. In Figs. 16 and 17 are shown a schematic of the AMS detector, the location of the AMS detector on the shuttle, and on the space station (ISSA). Figure 18 shows the expected improvement of the antimatter-matter ratio obtained by AMS after three years of running on ISSA.

5 PAMELA

PAMELA is part of the Russian Italian Mission (RIM) program, a collaboration between INFN and the VNIIEM Institute of Moscow with the participation of other international institutes, for sending cosmic ray telescopes into space as "piggy-back" on some of their satellites of the Resurs series.

The opportunity is unique both for the very favorable orientation of these satellites (looking to the Earth surface, and indeed out of the Earth on the other side) and for their polar orbit, allowing us to cover the whole energy range down to very low energies, highly enriching the possible physics program. Furthermore, their orbit is quasicircular at about 700 km, which guarantees a very long permanence in flight, and sun-syncronous, which maximizes the electric power availability.

The group headed by Prof. Arkady Galper, of the MEPI of Moscow, acted as interface with the VNIIEM Institute, so that in 1993 the Russian Italian Mission (RIM) program was established, of which the RIM-2 experiment, which we named PAMELA, is the central part.

5.1 The Technical Choices and the Baseline Design

The relative low magnetic field intensity due to use of a permanent magnet can be compensated with the progress made in the recent years in particle localization by the wide application of the silicon microstrip detectors.

The tests made in '94 and '95 of prototypes of the foreseen sensors for the PAMELA tracker guarantee the successful handling of this difficult technique.

The chosen cross section of the magnet gap is 14×16 cm^2, matching the optimal use of the four-inch silicon wafers to produce large area silicon microstrip sen-
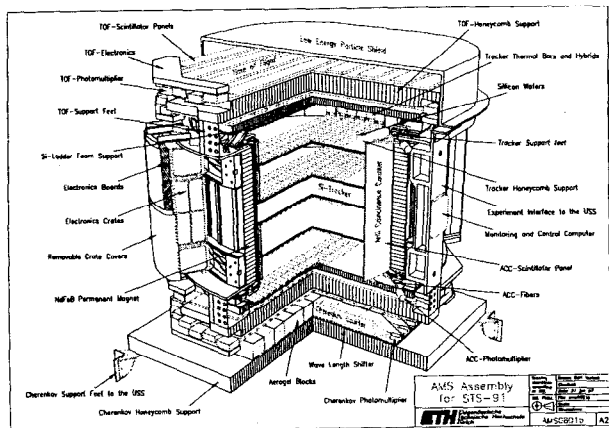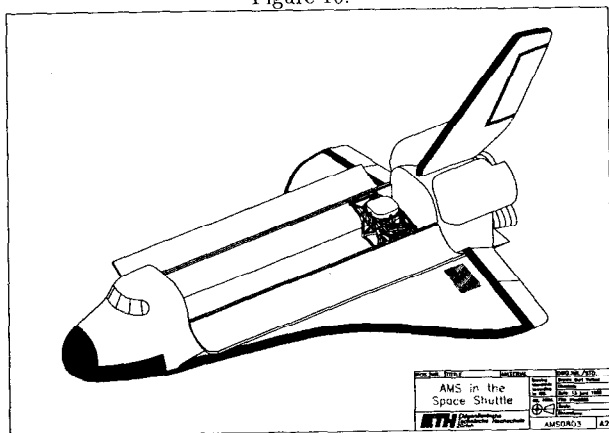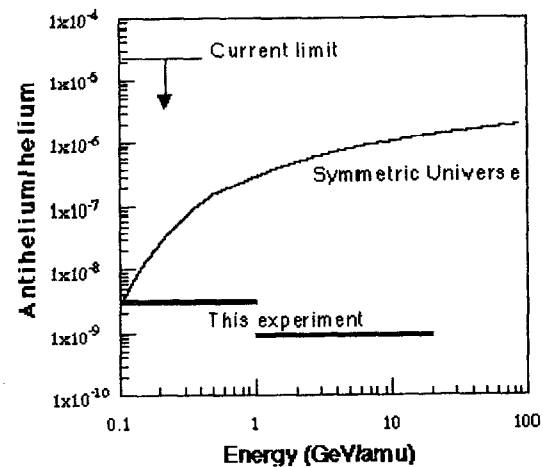
Figure 16.

Figure 17.

Figure 18: Expected improvements of the antimatter-matter ratio obtained by AMS after three years of running.

sors. For maximizing the MDR, we chose to have a relatively weak field ($\sim$0.35 T) on a relatively long magnetic path (44 cm, nearly the maximum allowed by the geometrical constraints to the experiment). The corresponding MDR is $\sim$ 370 GeV/c. The magnetic gap and the magnet length determine the angular acceptance of the telescope, $20.0° \times 17.7°$, corresponding to a geometrical acceptance of 24.5 cm^2 sr.

At low momenta, the MDR is dominated by the multiple scattering of the particle in the silicon sensors and in their supporting structures; afterward it increases linearly with the momentum.

The antiproton counting rate in the given GF is reported in Fig. 19 in two hypotheses: (1) only secondary produced antiprotons according to the Modified Leaky Box Model of the galaxy (MLBM) (lower curve); (2) only secondary produced antiprotons according to the Closed Galaxy Model (CGM). Any primary production mechanism will increase these rates. The counting rate foreseen for the positrons is reported in Fig. 20.

The technical choices for the other detectors are the following:

- silicon microstrip sensors for the imaging calorimeter, interleaved with tungsten plates as absorber; this choice minimizes the volume of the calorimeter
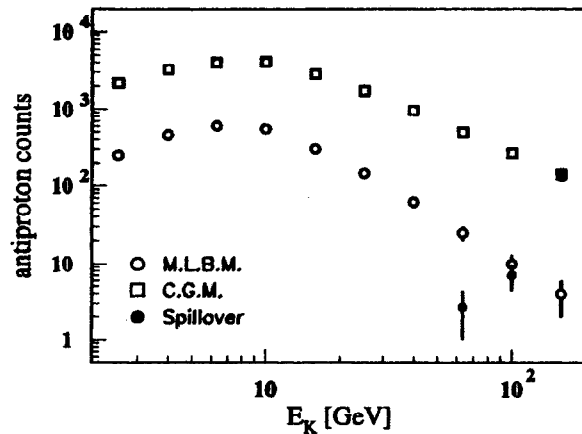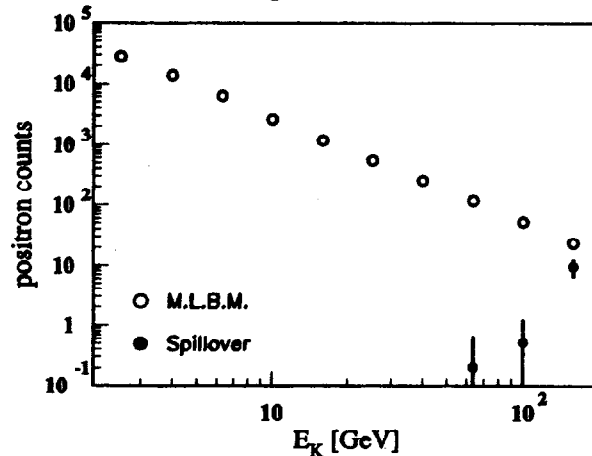
Figure 19.

Figure 20.

and maximizes indeed the geometrical acceptance; the high granularity assumed in PAMELA allows a very good separation between electromagnetic showers and interacting or not interacting hadrons; the chosen depth allows a good resolution in the measurement of the energy of electromagnetic particles, further extending the energy spectrum measurements of electrons and positrons;

● several scintillation counter hodoscopes for the construction of the triggers and for the TOF measurements; the use of several hodoscopes allows independent TOF measurements, improving the precision and the safety; the hodoscope structure maximizes the yield of the collected light and the safety of the system; both the hodoscopization and the number of hodoscopes allow a good flexibility in constructing the first-level triggers;

● a Transition Radiation Detector (TRD) for selecting electromagnetic particles from hadrons up to very high energy (∼1000 GeV); the TRD is based on small diameter straw tubes arranged in double layer planes interleaved by carbon fiber radiator. The use of the straw tubes allows us to perform many energy loss measurements along the particle trajectory (which brings the selection capability of the instrument down to less than 1 GeV), and to track all particles before their entrance in the magnetic spectrometer, cleaning the sample of the particles accepted at its entrance;

● a sixth scintillator layer will be located below the calorimeter as a penetration detector;

● finally, a set of scintillation counters covering the top edge and the sides of the magnetic spectrometer completes the telescope, for a further labeling of contaminated events.

The PAMELA telescope (see Fig. 21) consists of the following subdetectors (from the top to the bottom):

- two scintillation counter hodoscopes (S11 and S12);

- the TRD counter, occupying 29 cm in height;

- one scintillation counter hodoscope (CAT) on the top of the magnet, labeling the particles not entering the magnet gap;

- the magnet + tracker system, consisting of five permanent magnets, each 8 cm high, interleaving six detection planes of the silicon microstrip tracker,
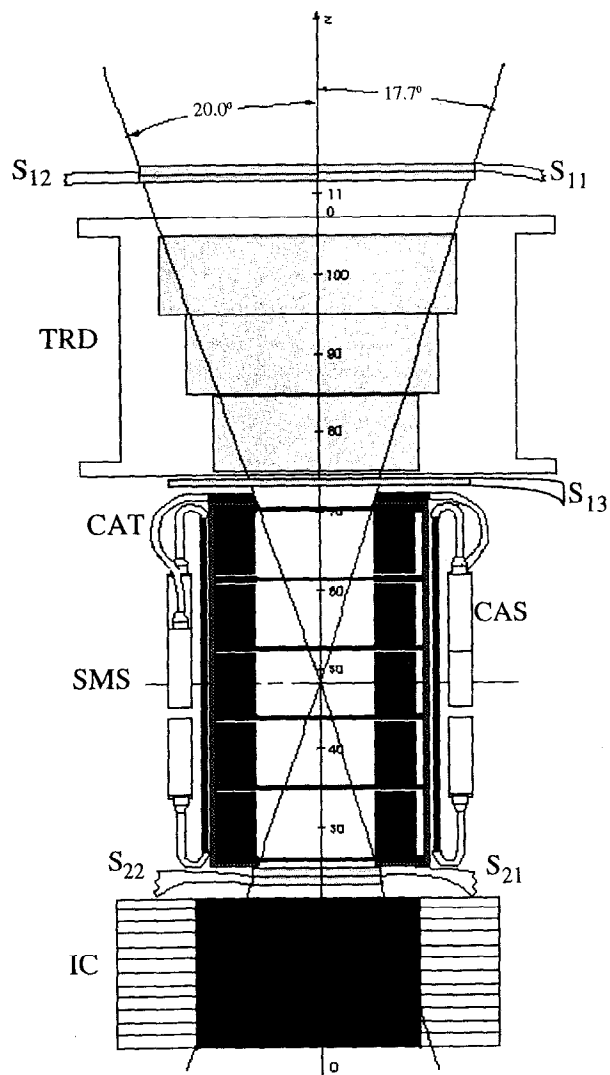
Figure 21: The PAMELA telescope.

each 0.8 cm high, enclosed in a ferromagnetic screen, 0.2 cm thick and surrounded on its sides by a system of scintillation counters (CAS) labeling the particles entering the spectrometer from the sides;

- two scintillation counter hodoscopes (S21 and S22);

- the imaging calorimeter, consisting of 23 planes of silicon microstrip sensors, interleaved by 23 tungsten sheets, whose physical occupancy in height is 19 cm.

The total height of the spectrometer is 113.5 cm. Tables 7 and 8 give technical parameters of PAMELA and the expected rate over the mission time (three years).

protons	3×10^8
antiprotons	$\geq 3 \times 10^4$
electrons	6×10^6
positrons	$\geq 3 \times 10^5$
He nuclei	4×10^7
Be nuclei	4×10^4
C nuclei	4×10^5
antinuclei limit (90% c.l.)	7×10^{-8}

Table 7: Expected rates in PAMELA in 10^8's.

6 Conclusion

Our understanding of the presence of antimatter in cosmic rays has recently progressed substantially. The future improvement will expand our knowledge, giving hopefully a conclusive result on the origin of antimatter in the universe.

Let me conclude this presentation by mentioning that GLAST (shown in Fig. 22), the next generation gamma ray (γ) telescope, will also contribute to solving the problem of the antimatter search in an indirect way by studying the diffuse γ spectrum, giving a limit to presence in the universe of regions where matter and antimatter are in contact on large scales, and give the typical γ spectrum from π^o decay modulated by the red shift due to the distance from our galaxy, as shown in Fig. 23 (De Rújula, 1996).

	Volume (xyz) (cm × cm × cm)	Mass (kg)	R.O.ch (#)	Power (W)
Scintillation counters	45×40×2 + 17×15×3 + 36×32×1	$\leq$33	34	$\leq$32
Trans. rad. detector	40×40×29	23	1,920	$\leq$40
Anticoincidences	(21×6×1)×4+ (9×30×1)×15+ (8×30×1)×5+	13	48	$\leq$5
Silicon tracker	(28×24×0.8)×6	10	36,864	37
Imaging calorimeter	30×24×19	129	3,312	$\leq$60
Fast trigger		5		10
General electronics		$\leq$15		25
Power supply		10		90
Permanent magnet	29×30×47 [(23×24×8)×5+ Fe shielding]	140		
General mechanical structure		25		
Total	45×40×114	$\leq$403	42,178	$\leq$299

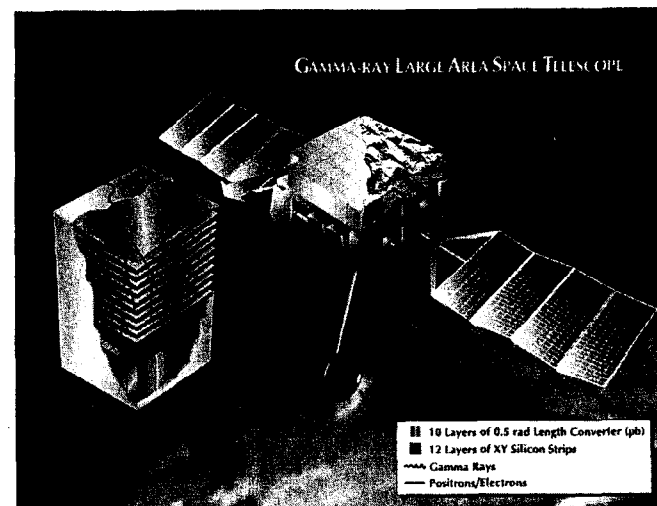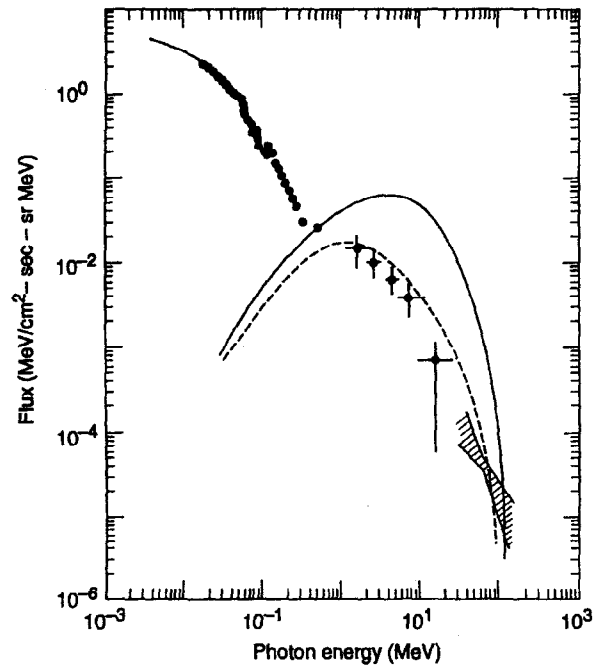Table 8: Main parameters of the elements of the PAMELA telescope.

Figure 22.

Figure 23: Comparision of the diffuse γ ray energy spectrum with the results of a matter/antimatter symmetric universe for d = Mpc. Dashed (continuous) lines are with (without) reheating by electrons and positrons from pp̄ annihilation.

References

- Adriani, O., *et al.*, *Proc. of XXIV ICRC*, Rome, **3**, 591 (1995).
- Agrinier, B., *et al.*, Lett. Nuovo Cimento **1**, 153 (1969).
- Barbiellini, G., *et al.*, Nucl. Instrum. Methods A **371**, 169 [1996(a)].
- Barbiellini, G., *et al.*, A&A **309**, L15 [1996(b)].
- Barwick, S. W., *et al.*, Phys. Rev. Lett. **75**, 390 (1995).
- Bocciolini, M., *et al.*, Nucl. Instrum. Methods A **333**, 77 (1993).
- Bocciolini, M., *et al.*, Nucl. Instrum. Methods A **370**, 403 (1996).
- Bogomolov, E. A., *et al.*, in *Proceedings of the XVI ICRC*, Kyoto, **1**, 330 (1979).
- Bogomolov, E. A. *et al.*, in *Proceedings of the XX ICRC*, Moscow, **2**, 72 (1987).
- Bogomolov, E. A. *et al.*, in *Proceedings of the XXI ICRC*, Adelaide, **3**, 288 (1990).
- Brun, R., *et al.*, "Detector Description and Simulation Tool," CERN program library (1994).
- Buffington, A., Schindler, S. M., and Pennypacker, C. R., Astrophys. J. **248**, 1179 (1981).
- Carlson, P., *et al.*, Nucl. Instrum. Methods A **349**, 577 (1994).
- Carlson, P., *et al.*, to appear in Nucl. Instrum. Methods (1995).
- University of Chicago, 1996, National Science Foundation Grant ATM-9420790, http://astro.uchicago.edu/home/web/pyle/neutron.html.
- Clem, J., *et al.*, in *Proceedings of the 24th Int. Cosmic Ray Conf.*, Rome, Vol. 3, **5** (1995).
- Daniel, R. R. and Stephens, S. A., Rev. Geoph. and Sp. Ph., Vol. 12, **233** (1974).
- Daugherty, J. K., *et al.*, Astrophys. J. **198**, 493 (1975).
- De Rújula, A., "Antimatter in the Universe?" CERN program library (1996).
- Fanselow, J. L., *et al.*, Astrophys. J. **158**, 771 (1969).
- Gaisser, T. K., and Schaeffer, R. K., Astrophys. J. **394**, 174 (1992).
- Gleeson, L. J., and Axford, W. I., Astrophys. J. **154**, 1011 (1968).
- Golden, R. L., *et al.*, Nucl. Instrum. Methods **148**, 179 (1978).
- Golden, R. L., *et al.*, Phys. Rev. Lett. **43**, 1264 (1979).
- Golden, R. L., *et al.*, Astrophys. Lett. **24**, 75 (1984).
- Golden, R. L., *et al.*, A&A **188**, 145 (1987).
- Golden, R. L., *et al.*, Nucl. Instrum. Methods A **306**, 366 (1991).
- Golden, R. L., *et al.*, Astrophys. J. **436**, 769 (1994).
- Golden, R. L., *et al.*, Astrophys. J. **457**, 103 (1996).

· Hof, M., *et al.*, Nucl. Instrum. Methods A **345**, 561 (1994).

· Hof, M., *et al.*, Astrophys. J. **467**, L33 (1996).

· Kiraly, P., Wdowczyk, J., and Wolfendale, A., Nature **293**, 120 (1981).

· Mitchell, J., *et al.*, Phys. Rev. Lett. **76**, 3057 (1996).

· Mitsui, T., Maki, K., and Orito, S., "Expected Enhancement of the Primary Antiproton Flux at the Solar Minimum," UT-ICEPP 96-03, 22 (1996).

· Moiseev, A., *et al.*, 1996, "Cosmic Ray Antiproton Flux in the Energy Range from 200 to 600 MeV," Astrophys. J., to appear in 1997.

· Muller, D., and Tang, K. K., Astrophys. J. **312**, 183 (1987).

· Papini, P., Grimani, C., and Stephens, S. A., Nuovo Cimento **19**, 367 (1996).

· Paradis, P., Ph.D. thesis, New Mexico State University, USA (1996).

· Pfeifer, C., Roesler, S., and Simon, M., Phys. Rev. C **54**, 2, (1996).

· Protheroe, R. J., Astrophys. J. **254**, 391 (1982).

· Rudaz, S., and Stecker, F. W., Astrophys. J. **325**, 16 (1988).

· Silk, J., and Srednicki, M., Phys. Rev. Lett. **53**, 624 (1984).

· Simon, M., *et al.*, Astrophys. J. **456**, 519 (1996).

· Stecker, F. W., Protheroe, R. J., and Kazanas, D., in *Proceedings of the XVII ICRC*, Paris, **9**, 211 (1981).

· Stecker, F. W. and Wolfendale, A. W., Nature **309**, 37 (1984).

· Stephens, S. A., in *Proceedings of the 17th Int. Cosmic Ray Conf.*, Paris, **282**, Vol. 4; *ibid.* **512**, Vol. 2 (1981).

· Stephens, S. A., "Secondary Antiproton Spectrum in the Atmosphere with the Inclusion of Fermi Motion in Air Nuclei," submitted to Astropart. Phys. (1996).

· Sullivan, J. D., Nucl. Instrum. Methods **95**, 5 (1971).

· Weber, N., 1996, "A measurement of the antiproton and proton fluxes in the cosmic rays by the CAPRICE experiment," Ph.D. thesis, KTH Stockholm, Sweden.